

ConvFeatNet ensemble: Integrating microstructure and pre-defined features for enhanced prediction of porous material properties

Yuhai Li ^a , Tianmu Li ^b, Longwen Tang ^a, Shiyu Ma ^{a,c} , Qinglin Wu ^a, Puneet Gupta ^{b,*} , Mathieu Bauchy ^{a,**}

^a Department of Civil and Environmental Engineering, University of California, Los Angeles, United States

^b Department of Electrical and Computer Engineering, University of California, Los Angeles, United States

^c Department of Statistics, Harvard University, United States

ARTICLE INFO

Keywords:

Porous materials
Fracture mechanics
Material properties prediction
SHAP analysis

ABSTRACT

This study introduces ConvFeatNet, a deep learning framework specifically designed to predict the mechanical properties of porous materials based on their microstructures. Despite dataset limitations, ConvFeatNet integrates both structural and predefined features with deep learning techniques to enhance predictive accuracy. The ensemble version of ConvFeatNet achieves a mean absolute error (MAE) of **0.85 J/m²** in predicting fracture energy using 1000 samples, outperforming a simple MLP (MAE: **1.08 J/m²**) and CNN (MAE: **1.38 J/m²**) by **21 %** and **38 %**, respectively. Expanding the dataset to 10,000 samples further reduces the MAE to **0.51 J/m²**, representing a **24 %** improvement over the MLP and a **9 %** improvement over the CNN. Additionally, SHAP analysis is employed to interpret model predictions, revealing the key structural determinants influencing mechanical behavior. This study highlights the synergy between deep learning and domain knowledge, offering a robust approach for deciphering the mechanical properties of porous materials.

1. Introduction

The mechanical behavior of materials with unique meso-, micro-, or nanostructures—such as pores [1], networks [2], layers [3], and inclusions [4]—diverges markedly under external loads compared to their homogenous solid counterparts. Recent advancements in manufacturing technologies, particularly autonomous and additive manufacturing, have enabled the fabrication of materials with intricately customized architectures across various scales [5,6]. These developments hold significant promise for structural engineering, aerospace, and biomedical applications, where the ability to precisely engineer material properties is essential for performance optimization and reliability. Despite these technological advances, the absence of a comprehensive model linking the structural characteristics of these materials to their macroscopic mechanical properties poses a significant barrier to their broader industrial application. The ongoing challenge of delineating the relationship between structure and property remains a central concern in materials science, despite substantial research efforts [7–9].

Traditionally, the field has leveraged physical principles to bridge

this gap, with varying degrees of success in specific systems due to the intricate dynamics of material deformation and fracture processes [10, 11]. Recent studies have demonstrated the potential of hybrid computational approaches that integrate physics-based models with machine learning (ML) to improve predictive accuracy while maintaining interpretability [12–16]. Notably, Physics-Informed Neural Networks (PINNs) have gained attention for their ability to incorporate governing equations into ML frameworks for improved material property predictions, offering an efficient alternative to conventional finite element simulations [12]. Moreover, deep learning techniques have been applied to predict fracture behavior in high-carbon steels, enabling tailored design strategies for improved mechanical performance [17].

ML has shown considerable potential across diverse research areas [18–24]. The Multilayer Perceptron (MLP), a fundamental ML technique, has been particularly effective in material science for modeling the intricate relationships between input attributes and mechanical properties. It converts extensive experimental and simulation data into feature vectors, facilitating the efficient learning of structural-property links [25,26]. MLPs demonstrate remarkable predictive accuracy when

* Corresponding author.

** Corresponding author.

E-mail addresses: puneetg@ucla.edu (P. Gupta), bauchy@g.ucla.edu (M. Bauchy).

sufficiently trained with data that encapsulate significant structural characteristics [27,28]. However, their performance can be limited by feature engineering, which may not capture all critical microstructural variations.

Conversely, Convolutional Neural Networks (CNNs) excel in processing two-dimensional (2D) or three-dimensional (3D) images and have been beneficial for studying materials like brittle substances and composites [29–32]. Recent advancements in adaptive CNN architectures have further improved the prediction of material properties by dynamically adjusting weight distributions based on hierarchical feature learning [33]. However, CNNs often require large training datasets to generalize well, making them less effective in scenarios where data is limited. Furthermore, the “black box” nature of these models often limits deeper interpretive analyses of their internal workings.

Addressing these gaps, our study introduces a novel hybrid model that synergistically combines MLP and CNN architectures. This approach effectively mitigates the data-intensive demands of CNNs by coupling them with an MLP trained on predefined features, thereby enhancing the capture of critical structural information even under limited data conditions. Additionally, ensemble learning has been shown to significantly boost predictive robustness, as multiple deep learning models can reduce variance and improve reliability in property prediction for heterogeneous materials [34]. By integrating these strategies, our methodology not only achieves high accuracy across varying dataset sizes but also has the potential to accelerate the design and optimization of advanced materials, a key priority in industries such as additive manufacturing and structural engineering.

Further, our analysis incorporates Shapley Additive Explanations (SHAP) [35], which elucidate the influence of specific structural features on predicted mechanical properties like Young’s modulus, strength, and fracture energy. Recent work in explainable AI (XAI) has underscored the importance of interpretability in materials science, bridging the gap between data-driven predictions and physical understanding [16]. SHAP values, grounded in cooperative game theory, quantify the contribution of each feature to the model’s predictions, offering insights into how these features affect material behavior. This interpretability is particularly relevant for industrial applications, where transparent, evidence-based decision-making can guide manufacturing processes and component design. By combining domain expertise with state-of-the-art ML techniques, our study provides a robust framework for understanding and predicting the mechanical properties of porous materials—benefiting sectors ranging from additive manufacturing to aerospace and civil infrastructure.

2. Method

2.1. Simulation

The simulation component of this study employed the Linear State-based Peridynamic Solid (LPS) model as its constitutive framework due to its superior capability in modeling fracture mechanics without requiring additional assumptions about crack initiation and propagation. Unlike classical continuum mechanics models, which rely on partial differential equations (PDEs) and often struggle with discontinuities, the peridynamic approach inherently accommodates the formation and evolution of cracks without requiring predefined crack paths. This feature is particularly advantageous for porous materials, where the presence of voids and complex microstructures makes fracture behavior highly unpredictable.

Other alternative models, such as finite element-based cohesive zone models (CZM) or phase-field models, are widely used for fracture mechanics simulations. However, these methods typically require explicit definition of fracture criteria, mesh-dependent crack propagation strategies, or computationally expensive phase-field regularization terms. In contrast, the LPS model naturally captures nonlocal interactions and allows for a more realistic representation of the failure process in porous

materials, where microstructural heterogeneity significantly influences mechanical response. Furthermore, peridynamics has been successfully applied in multiscale modeling of brittle and quasi-brittle materials, making it an ideal choice for this study.

To accurately represent the porous material’s structure, we modeled it as a grid system composed of unit cells, categorized either as solid or void based on the predefined porosity levels. This approach allows for precise manipulation of the material’s internal structure to investigate various porosity impacts on mechanical properties.

For the mechanical testing simulations, the specimens were configured to experience single-edge notched stress conditions. The initial notch, highlighted by a red line in Fig. 1(a), spanned five unit cells, with each cell maintaining an edge length of ten lattice spacings. Notably, setting the lattice spacing to 15 nm facilitated a convergence in the resultant stress-strain curves, indicative of the model’s robustness in simulating realistic material responses. The chosen thickness of the material, ten lattice spacings, was found adequate to ensure consistent results in the system’s elastic response. Furthermore, the horizon was set to three times the lattice spacing, optimizing the interaction range within the peridynamic model.

To balance computational efficiency with simulation accuracy, the experiment was conducted at a strain rate of 10^5 s^{-1} . This specific condition was selected to closely emulate practical load rates while maintaining computational manageability. For a comprehensive understanding of the simulation setup and its integration with the overarching research objectives, further details can be found in our previous work [36], which provides an in-depth examination of the peridynamic simulation processes employed.

While the peridynamic approach offers advantages in capturing complex failure mechanisms, the simulation setup is subject to several limitations. First, the peridynamic model is computationally expensive compared to traditional finite element methods (FEM). The need for nonlocal interactions requires a larger computational domain, increasing the number of equations to be solved. In this study, each simulation took approximately 2.5–4 h on a 16-core CPU, which limits the feasible dataset size. Future work could incorporate GPU acceleration or reduced-order modeling techniques to improve efficiency. Second, the strain rate in the simulation was chosen based on computational feasibility rather than exact experimental conditions. Although selected to balance computational efficiency with mechanical accuracy, the strain rate may affect the predicted fracture energy, particularly in materials exhibiting rate-dependent behaviors. Future validation against experimental results at multiple strain rates would further refine model accuracy. Third, the porous material was modeled as a uniform grid of solid and void unit cells, which is a simplification of real-world materials. Natural porous structures often exhibit irregular pore shapes and size distributions, which can influence mechanical behavior. While our feature extraction process captures these effects to some extent, incorporating randomized pore distributions or experimentally derived microstructures would enhance realism. Lastly, the notched specimen setup simplifies fracture initiation and propagation under uniaxial tension. In practical applications, materials experience multi-axial loading conditions or complex stress states that may alter failure behavior. Future work could explore mixed-mode fracture simulations to account for real-world loading scenarios.

2.2. Data

The primary objective of this research was to develop computational models capable of accurately predicting three fundamental mechanical properties derived from stress-strain curves: Young’s modulus, tensile strength, and fracture energy. Young’s modulus (E) quantifies a material’s resistance to axial deformation under external force, representing the proportionality between tensile/compressive stress (σ) and axial strain (ϵ) within the linear elasticity domain of the material. The value of E is pivotal for understanding material behavior under load [37]. Tensile

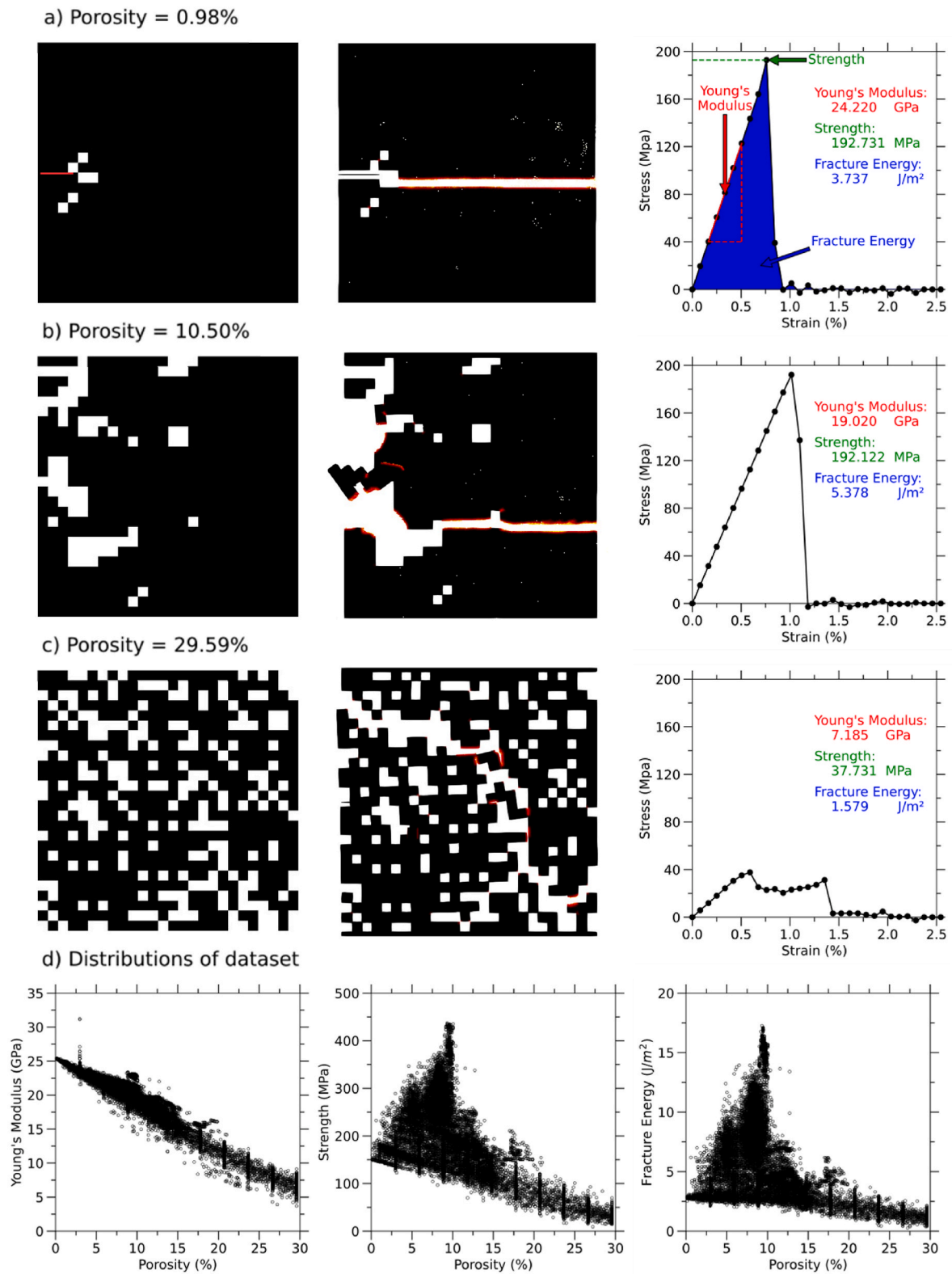


Fig. 1. Visualization of Porosity and Fracture Patterns in Porous Materials. (a) Shows a microstructure with a low porosity (0.98%), displaying a linear fracture trajectory. (b) Illustrates a microstructure with moderate porosity, showcasing non-linear crack propagation and branching. (c) Depicts a highly porous microstructure with scattered cracking patterns. This figure also includes stress-strain curves for each configuration, demonstrating how porosity influences mechanical properties. (d) Provides a graphical representation correlating the three physical properties (Young's modulus, tensile strength, and fracture energy) with varying porosity levels across the dataset.

strength defines the critical juncture on the stress-strain curve where permanent deformation occurs post-load application. Fracture energy, denoted as $G_f = \int_0^{\epsilon_f} \sigma(\epsilon) d\epsilon$, measures the energy required to propagate a fracture surface, equating to the area under the stress-strain curve up to the fracture point [38]. This metric correlates the expended energy to the dimensions of the fractured area [39].

To facilitate these analyses, a dataset comprising 10,000 layouts reflecting varying porosity rates from 0 % to 30 % was constructed. Fig. 1(a)–(c) illustrates these grids that exhibit different levels of porosity, processed through a peridynamic simulator [40], which simulates the mechanical responses of materials under uniaxial load conditions, such as crack formation.

The construction of the porous microstructure involved selectively removing solid cells to create voids, thereby varying the porosity. The subsequent simulations of uniaxial tensile fracture on these structures provided insights into fracture mechanics as influenced by porosity variations. Fig. 1(a)–(c) present the initial microstructures, the resultant fracture patterns, and the corresponding stress-strain curves. For instance, the microstructure with the lowest porosity (0.98 %) exhibited a linear fracture trajectory and demonstrated brittle fracture behavior, as evidenced by a sharp decline in stress post-peak stress in Fig. 1(a). Conversely, higher porosity samples, like the one in Fig. 1(c), showed diverse cracking patterns due to the presence of significant natural voids, influencing crack propagation and demonstrating instances of strain hardening and ductile fracture behavior.

In-depth analysis revealed a pronounced negative linear correlation between Young's modulus and porosity, while the relationships with strength and fracture energy were more complex, as depicted in Fig. 1 (d). The scatter plots indicate that mid-range porosity levels show significant variability, suggesting that the location and distribution of pores play a crucial role. These observations imply that porosity alone is not a sufficient predictor of material properties; instead, the spatial arrangement of pores must also be considered to fully understand their impact

on mechanical behavior.

As the study delved deeper into the complexities of material topography, a rigorous feature extraction process was initiated to distill the complex microstructure architectures into fundamental geometric attributes suitable for machine learning analysis. Eleven critical geometric features were identified, tailored to encapsulate not only the basic microstructure properties but also to enhance the predictive capabilities of machine learning algorithms by capturing the nuanced relationships between microstructural features and mechanical properties. This initiative significantly improved our understanding and modeling of material behavior, integrating empirical knowledge with computational intelligence. Further details on these features and their implications for machine learning performance are elaborated in Supplementary Note 1.

2.3. Model architectures

This section delineates four sophisticated models visualized in Fig. 2, which are employed for predicting the physical properties of materials. These models—multilayer perceptron (MLP), convolutional neural networks (CNN), convolution-feature network (ConvFeatNet), and ConvFeatNet ensemble—are optimized using the Adam optimizer [41], targeting minimal mean-square error (MSE). Prior to training, data is segregated into an 80 % training set and a 20 % validation set through stratified random sampling. Model performance is evaluated based on root-mean-square error (RMSE), mean absolute error (MAE), and the coefficient of determination (R^2), ensuring robust validation of predictive accuracy.

2.3.1. MLP

The MLP model, structured as a directed acyclic graph of layers, features a sequence of four dense layers with dimensions of 512, 128, 64, and 32, employing rectified linear units (ReLU) as activation functions (Fig. 2(a)). This architecture allows the MLP to leverage its nonlinear

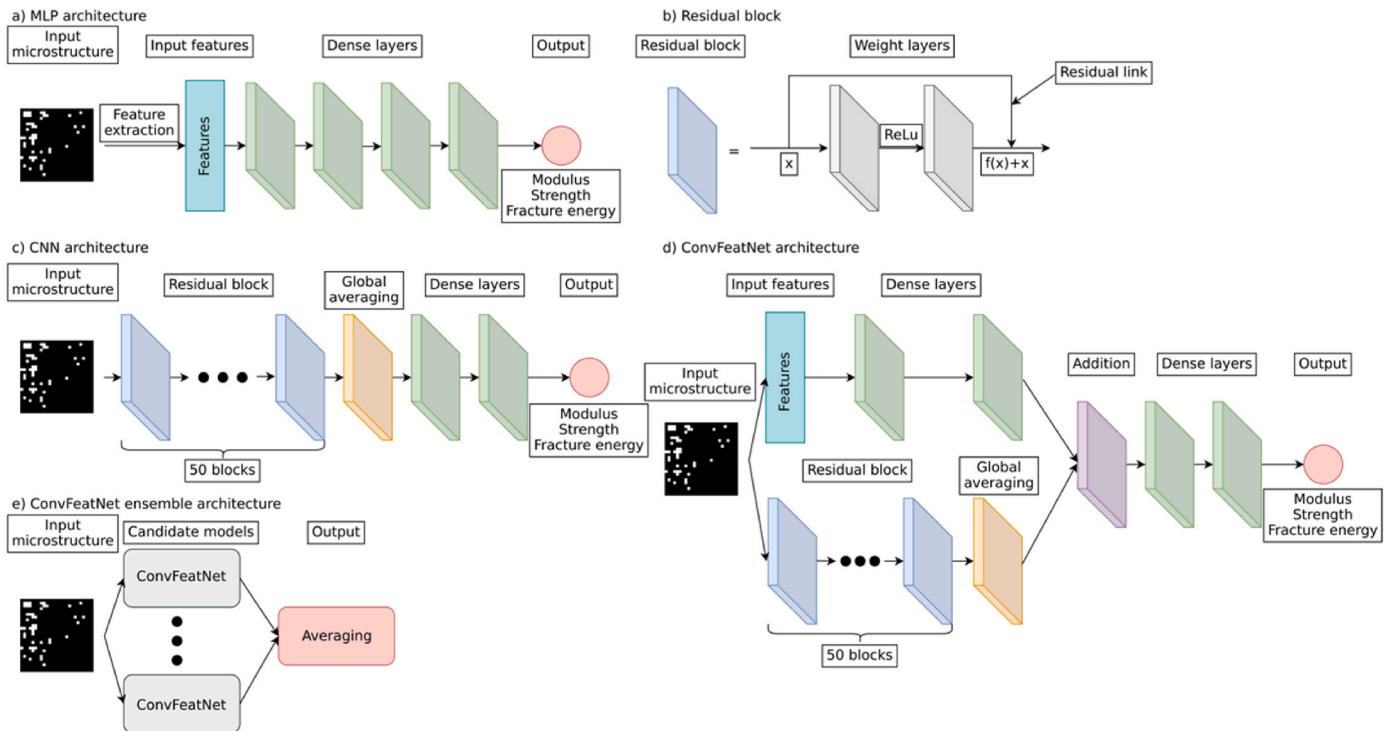


Fig. 2. Architectural Overview of Predictive Models Used in the Study. This figure visualizes the distinct configurations of the four models employed for material property prediction. (a) Displays the multilayer perceptron (MLP) setup, consisting of a linear stack of four dense layers. (b) Highlights the residual block, a series of convolutional layers with a skip connection. (c) Illustrates the convolutional neural network (CNN) using the ResNet architecture. (d) Depicts the ConvFeatNet model, showcasing its dual-input structure with both MLP and CNN branches. (e) Shows the ConvFeatNet ensemble approach, emphasizing the integration of multiple ConvFeatNet models to enhance prediction stability and reduce variance.

fitting capabilities to predict physical properties from input microstructural features, encapsulating knowledge within the layer weights. The motivation behind employing MLP lies in its ability to rapidly process features into predictions, making it invaluable for preliminary assessments where quick insights into material properties are crucial.

The choice of the MLP architecture was primarily guided by our hypothesis that input feature quality has a greater impact on MLP performance than the specific model architecture. First, given that fracture energy is the most challenging property to predict (compared to Young's modulus and strength), we focused on optimizing the model specifically for this task. In our experiments, we systematically varied the number of dense layers and the number of neurons per layer, finding that these modifications resulted in only marginal improvements ($\sim \pm 0.03$ MAE on the predicted fracture energy) when models were properly trained to avoid overfitting. This suggests that the MLP's predictive performance is constrained more by the effectiveness of feature engineering rather than network depth. While we acknowledge that an optimal MLP architecture could potentially improve performance, exhaustive enumeration of all possible architectures was not the primary focus of this study. Instead, our design choice prioritizes robust feature extraction and structured learning over architectural tuning, which aligns with our objective of generalizable property prediction.

2.3.2. CNN

Utilizing the renowned ResNet architecture, our CNN model incorporates multiple residual blocks to enhance deep learning (Fig. 2(b)). This model, grounded in the ResNet-50 architecture with a foundation of 50 residual blocks, employs Xavier initialization to optimize training [42]. Designed to process graphical representations of input microstructures, the CNN excels at detailed image-based analysis, making it particularly effective for capturing subtle textural features of materials that are critical for accurate property prediction.

Our initial experiments with CNN models containing only a few convolutional layers showed that they tended to underfit, especially when predicting fracture energy. This suggests that a deeper network was necessary to extract meaningful patterns from the microstructure images. Since residual networks (ResNets) are designed to train deep models efficiently by addressing vanishing gradient issues and allow to train a deeper model, we explored various ResNet architectures to find the best balance between accuracy and computational efficiency.

To determine the optimal ResNet depth, we compared the performance of ResNet-18, ResNet-34, ResNet-50, and ResNet-101 on our dataset. The digits represent the number of residual blocks. Our results, detailed in the Supplementary Note 3, show that ResNet-18 and ResNet-34 were too shallow and failed to capture critical microstructural features, leading to underfitting. On the other hand, ResNet-50 significantly improved accuracy, while ResNet-101 did not provide further performance gains but substantially increased training time. Given this trade-off, ResNet-50 was selected as the optimal choice, offering a good balance between model complexity, training time, and predictive accuracy.

While we recognize that other architectures might improve performance, exhaustive architecture optimization is not the focus of this study. Instead, we prioritized selecting a well-established deep CNN model that could effectively learn from microstructural images without excessive computational overhead. Future work could explore automated architecture search or alternative CNN designs to refine the model further.

2.3.3. ConvFeatNet

ConvFeatNet is designed to overcome the inherent limitations of both MLP and CNN. While MLPs are constrained by the quality of extracted features, CNNs require large datasets to function well. By merging elements of both models, ConvFeatNet enhances prediction accuracy across diverse datasets, making it a robust solution for material property analysis.

As depicted in Fig. 2(d), ConvFeatNet features a dual-branch

architecture. The first branch, an MLP, is finely tuned to analyze and interpret the extracted features, capitalizing on its strength in handling structured data. The second branch, based on the ResNet-50 architecture, processes microstructures, utilizing its depth to capture complex patterns in image data. This bifurcation allows each branch to operate within its strengths, creating a synergistic effect once their outputs are integrated.

The outputs from both branches are fed into a regressor consisting of two densely connected layers, harmonizing the insights gained from both feature analysis and image processing. If the MLP branch were removed, ConvFeatNet would function purely as a CNN; conversely, removing the CNN branch would leave a standalone MLP system. A key preliminary step involves normalizing the output weights from both branches to ensure consistency and compatibility in their integration.

The innovation of ConvFeatNet lies in its unique training methodology. Initially, the CNN branch's weights are set to zero, rendering it untrainable. During this early phase, only the MLP branch is active, and its output, combined with the regressor, contributes to the loss function. This approach allows the MLP branch to stabilize based on the extracted features without interference from the CNN outputs, establishing a robust baseline prediction capability.

Formally, let y be the true value, h_{MLP} be the feature vector output from the MLP branch, and h_{CNN} be the feature vector output from the CNN branch. During the initial phase, the loss function L can be expressed as:

$$L = \frac{1}{N} \sum_{i=1}^N \left(y_i - f_{regressor}(\alpha h_{MLP,i}) \right)^2$$

where N is the number of training samples, and α is the weight assigned to the MLP branch's output. At this stage, β (the weight for h_{CNN}) is set to zero, effectively excluding the CNN branch from the loss function:

$$h = \alpha h_{MLP} + \beta h_{CNN} \text{ with } \beta = 0$$

As training progresses, the CNN branch is set to trainable, allowing it to learn directly from the microstructures. The weight β is progressively increased from zero, allowing the CNN's contributions to grow. The updated loss function at this stage is:

$$L = \frac{1}{N} \sum_{i=1}^N \left(y_i - f_{regressor}(\alpha h_{MLP,i} + \beta h_{CNN,i}) \right)^2$$

Here, $f_{regressor}$ denotes the regression function that combines the weighted outputs of the MLP and CNN feature vectors to make the final prediction.

The training protocol assigns 200 epochs to this sequential activation process, managing the knowledge transfer from MLP to CNN. This staged learning approach ensures that the MLP branch stabilizes first, effectively handling the extracted features, while the CNN branch is progressively incorporated to enhance the model's capacity. As the CNN branch directly extracts features from the input microstructure, it complements the MLP branch by mitigating the information gap between the true values and the MLP's predictions. When sufficient data is available, the CNN's substantial representational power captures complex visual patterns, thereby enhancing the overall model accuracy and robustness.

This dynamic interplay between MLP and CNN within ConvFeatNet allows for a comprehensive learning process. Initially, the system focuses on mastering a straightforward representation of the input ($f(x)$), as understood by the MLP. The CNN then steps in to refine this understanding, adjusting for any discrepancies in the initial model's predictions ($f(x) - fa(x)$), where $fa(x)$ represents the approximation provided by the MLP. This layered learning structure ensures that ConvFeatNet not only learns effectively across varying scales of data complexity but also adapts to the intricate dynamics of material properties.

2.3.4. ConvFeatNet ensemble

The ConvFeatNet ensemble addresses challenges inherent to models trained on limited datasets, specifically high variance, and susceptibility to overfitting. Ensemble methods are recognized for their ability to enhance model robustness and accuracy by aggregating the outputs of multiple models. Following the approach outlined in Ref. [43], this ensemble strategy leverages six instances of the ConvFeatNet, each initialized differently to capture a diverse range of data patterns and anomalies. The aggregation of the model outputs is performed through averaging, which helps to smooth out individual model errors and improve overall prediction accuracy.

To construct the ensemble, we replicate the ConvFeatNet training process using the same dataset across six different model initializations. This number is strategically chosen based on empirical evidence suggesting that increasing the number of models beyond six yields diminishing returns in terms of performance enhancement. Each model in the ensemble undergoes training simultaneously within the same computational environment to ensure consistency in data handling and processing conditions.

Upon completion of the training phase, we undertake a rigorous evaluation of each model's performance. Models exhibiting training losses that exceed a predetermined empirical threshold—derived from historical performance data on similar tasks—are systematically excluded from the ensemble. This selection criterion is crucial for maintaining the quality and reliability of the ensemble predictions by ensuring only the most effective models contribute to the final output.

The outputs of the remaining models are then averaged, a method proven to reduce variance and mitigate the risk of overfitting. This averaging process harmonizes the individual strengths and idiosyncrasies of each model, leading to a more stable and reliable prediction output. The performance of the ensemble is subsequently assessed using established metrics such as MAE and RMSE, providing a comprehensive evaluation of its predictive accuracy and generalizability.

By integrating multiple models, the ConvFeatNet ensemble not only addresses the limitations posed by small datasets but also enhances the predictive capacity of the system, making it exceptionally adept at handling complex predictive tasks where single models might falter due to data paucity.

2.4. Workflow

The flowchart in Fig. 3 depicts how we generate microstructures, perform peridynamic simulations, parse input features, and train the MLP, CNN, and ConvFeatNet models (including the ensemble version).

We begin by generating porous microstructures with varying void distributions. Each microstructure is simulated via the LPS model to capture fracture dynamics. The resulting stress-strain curves serve as ground truth for mechanical properties. We parse the microstructure

grid to extract key features (e.g., porosity, spread), which become inputs for the MLP. Meanwhile, the CNN directly processes the microstructure images. ConvFeatNet combines both extracted features and image data. All models output the predicted physical properties (Young's modulus, strength, fracture energy). The predictions are compared against the ground truth derived from the LPS-simulated stress-strain curves, and an MSE loss is calculated. The MSE loss is then backpropagated to update each model's parameters.

2.5. SHAP analysis

To interpret the contribution of different input features in our models, we applied SHAP to both the standalone MLP model and the MLP branch within ConvFeatNet. SHAP is a widely used method for explaining machine learning predictions by quantifying the impact of each input feature on the model's output. This allowed us to assess how the MLP-based models leverage predefined structural features when predicting material properties.

For the standalone MLP model, SHAP was applied to evaluate the importance of each input feature when predicting Young's modulus, tensile strength, and fracture energy. This analysis helped us understand which predefined microstructural characteristics contributed the most to the model's predictions. For ConvFeatNet, we performed SHAP analysis specifically on the MLP branch, which processes numerical structural features, separate from the CNN branch that handles microstructural images. This helped determine how the structured features were utilized within the hybrid model.

It is important to note that in our study, SHAP analysis was used solely as an interpretability tool and did not influence our feature selection process. The features used in our models were chosen based on domain knowledge and prior research, rather than being optimized using SHAP results. While SHAP provides valuable insights into how the model makes predictions, it was not used to refine the feature set or adjust model architecture.

By incorporating SHAP into our analysis, we ensure that our models remain interpretable, allowing us to verify that they are making predictions based on meaningful structural features. This approach enhances transparency and helps establish confidence in the model's ability to generalize to unseen data.

3. Results and discussion

3.1. Learning curves analysis

In this section, we delve into the resilience and adaptive capacity of our proposed models by scrutinizing how they perform as more training data is incorporated into the property prediction process. This analysis not only identifies general trends across three key material properties

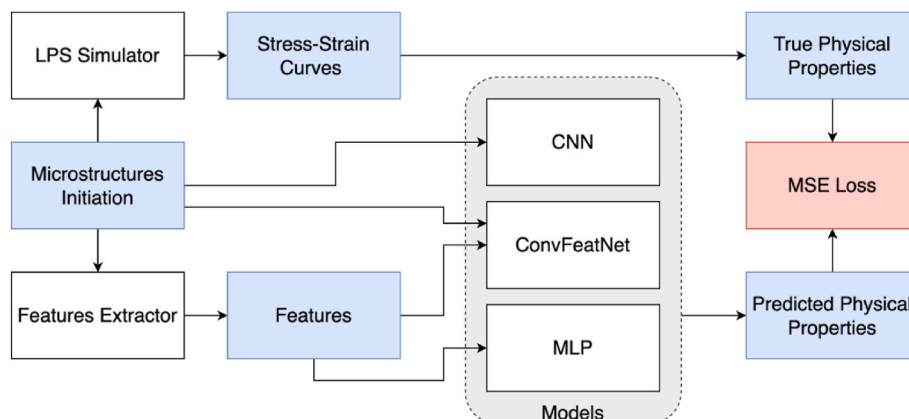


Fig. 3. Flowchart illustrating the end-to-end process of microstructure generation, peridynamic simulation, feature extraction, and model training.

but specifically accentuates fracture energy, with further details on the other properties accessible in Supplemental Note 2.

3.1.1. Comparative Performance Analysis of MLP, CNN, and ConvFeatNet

The analysis of training and validation curves, as illustrated in Fig. 4 (a)(i) and 4(b)(i), reveals a consistent decline in MSE across all models, indicating effective learning and adaptation to the data. Initially, with smaller datasets, the MLP and ConvFeatNet exhibit superior performance over the CNN, suggesting their robustness in scenarios with limited data. However, as the volume of data increases, the CNN demonstrate significant improvements and begin to outperform the MLP in reducing MSE, while ConvFeatNet maintains a performance level comparable to CNN, benefiting from its hybrid architecture.

This nuanced performance dynamic is further explored through parity plots in Fig. 4(c)(i) – 4(c)(iii) and 4(d)(i) – 4(d)(iii), which provide a detailed view of how each model's predictions align with actual values across different dataset sizes. Notably, at 10 % training data usage, both MLP and ConvFeatNet outperform CNN across all evaluation metrics. This trend illustrates the efficacy of MLP and ConvFeatNet in managing small datasets effectively. However, certain variations in prediction accuracy are observed, particularly in the fracture energy range of 5 J/m² to 12.5 J/m², where the models encounter some challenges.

The integration of MLP and CNN within the ConvFeatNet architecture moderates and enhances the predictions from both models, leading to improved accuracy in various scenarios. This synthesis of methodologies results in a comprehensive model that leverages the strengths of its components to enhance overall performance. When the full training set is utilized, as shown in Fig. 4(d), MLP demonstrates increased accuracy in specific energy zones, highlighting the potential of predetermined

features to enhance prediction accuracy. Conversely, CNN's performance markedly improves with larger datasets, showcasing its capability to handle complex data structures and extract intricate patterns effectively.

The investigation into the operational characteristics of MLP, CNN, and ConvFeatNet offers valuable insights into their individual strengths and potential limitations. MLP's primary advantage lies in its use of predetermined features, which enable rapid and accurate predictions when data volume is constrained. Data volume may be constrained due to the computational intensity of LPS simulations required to generate the dataset. Based on our experiments, each simulation takes approximately 2.5–4 h on a 16-core CPU or 4–6.5 h on an 8-core CPU. This significant time investment limits the amount of data that can be feasibly generated. However, while the MLP performs well with smaller datasets, its reliance on predetermined features restricts their adaptability to more complex datasets where variable relationships may be intricate and non-linear.

In contrast, CNN excels as it scales up, learning from a broad array of data inputs to unveil complex patterns, albeit with an initial susceptibility to bias and variance. This makes CNN particularly powerful in environments rich in data, where its depth and complexity can be fully leveraged.

ConvFeatNet stands out by combining the quick adaptability of MLP to structured data with the deep learning prowess of CNN, which excels in image and pattern recognition. The training approach for ConvFeatNet is distinctively designed to first stabilize the MLP outputs before gradually integrating the CNN's capabilities. This phased learning strategy ensures robustness and flexibility, allowing ConvFeatNet to provide reliable predictions across varying data volumes

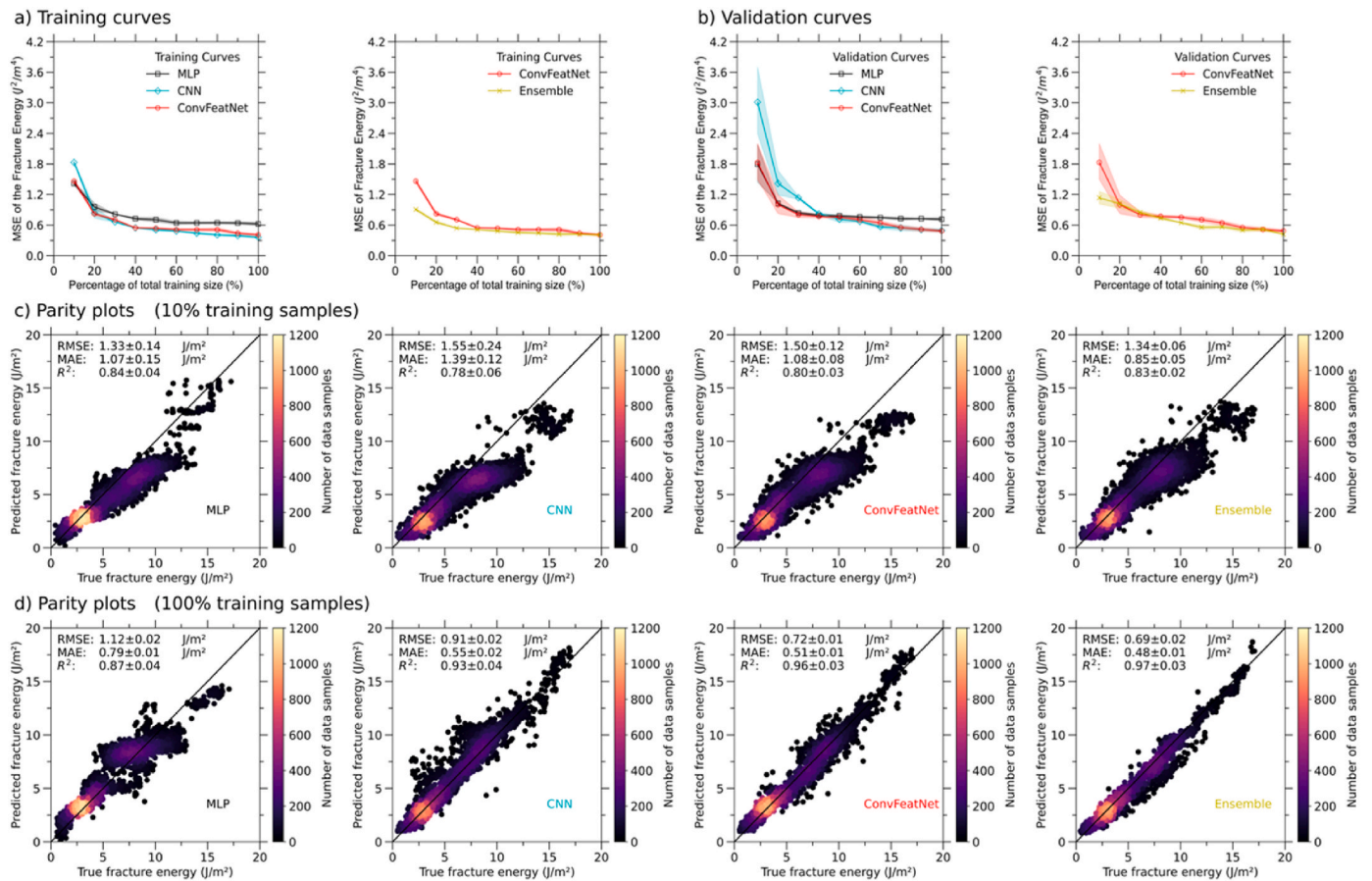


Fig. 4. Comparative Performance Analysis of MLP, CNN, and ConvFeatNet. (a) Training-set learning curves for all models (MLP, CNN, ConvFeatNet, and ConvFeatNet Ensemble) under varying training sample sizes (10%–100%). (b) Corresponding validation-set learning curves. (c) Parity plots for all models when 10 % of the dataset is used for training. (d) Parity plots when the full (100 %) dataset is used for training.

and complexities.

Overall, the comparative analysis underscores the complementary nature of the models. ConvFeatNet, by integrating the strengths of both MLP and CNN, presents a balanced approach to tackling different challenges posed by the dataset size and complexity. This hybrid model not only adapts to the available data but also optimizes the extraction and utilization of information.

3.1.2. Comparative Performance Analysis of ConvFeatNet and ConvFeatNet ensemble

To further improve the predictive performance of ConvFeatNet, we have developed an ensemble version of the model. Analysis of the training curves, as detailed in Fig. 4(a) and (b), reveals that the ConvFeatNet ensemble demonstrates more consistent and stable performance, with notably less variation in results compared to the standalone model. This stability is particularly evident in the mid-energy range (5 J/m² to 12.5 J/m²) as shown in the parity plots of Fig. 4(c) and (d).

The ensemble approach effectively aggregates the predictive capabilities of multiple ConvFeatNet instances, each trained under different initializations. This strategy not only mitigates the risk of overfitting—a common challenge in complex neural network architectures—but also enhances the generalizability of the model across diverse datasets. By averaging the outputs of several models, the ensemble is able to smooth out anomalies and reduce bias that may be present in individual predictions.

The ensemble's consistent performance across varied energy ranges highlights its capacity to deliver reliable outcomes, even under fluctuating training conditions. The enhanced learning curves and decreased variance underscore the robustness of the ensemble approach, ensuring that the model remains effective despite potential variations in input data quality or volume.

3.1.3. Statistical significance of performance improvements

To validate that the performance improvements of our models are statistically significant, we conducted paired t-tests on the MAE results obtained from a 5-fold cross validation for fracture energy prediction. In our experimental setup, we used a stratified split based on the target physical property value, ensuring that 80 % of the data was used for training and 20 % for testing in each fold. Each model was trained individually on the identical training set and evaluated on the identical testing set. Table 1 summarizes the MAE values (in J/m²) for fracture energy from each fold (the results for Young's modulus and tensile strength are provided in the supplementary material).

For a given pair of models (e.g., MLP and ConvFeatNet), we computed the difference in MAE for each run and then used these differences as input to the paired t-test. Formally, if d_i is the MAE difference (Model A minus Model B) in run i for $i = 1, 2, \dots, n$, the test statistic is:

$$T = \frac{\bar{d}}{s_d / \sqrt{n}}$$

where \bar{d} is the mean of the differences, s_d is the standard deviation of the

Table 1
MAE values for fracture energy from 5-fold cross-validation.

Fold	MLP (J/m ²)	CNN (J/m ²)	ConvFeatNet (J/m ²)	ConvFeatNet Ensemble (J/m ²)
1	0.80	0.54	0.52	0.49
2	0.81	0.55	0.51	0.48
3	0.78	0.53	0.50	0.47
4	0.79	0.59	0.52	0.48
5	0.78	0.55	0.50	0.47
Mean	0.79	0.55	0.51	0.48
Standard Deviation	0.01	0.02	0.01	0.01

differences, and n is the number of runs (here, $n = 5$). A p-value <0.05 indicates that the difference in performance between the two models is statistically significant at the 95 % confidence level.

Table 2 shows the p-values from 5 key comparisons: MLP vs. ConvFeatNet, CNN vs. ConvFeatNet, MLP vs. ConvFeatNet Ensemble, CNN vs. ConvFeatNet Ensemble, and ConvFeatNet vs. ConvFeatNet Ensemble. All tests confirm that ConvFeatNet and its ensemble version achieve significantly lower MAE than the baseline models.

The low p-values (<0.05) in Table 2 confirm that the improvements offered by ConvFeatNet and its ensemble variant are statistically significant, reinforcing the conclusion that these models outperform simpler architectures in predicting fracture energy.

3.2. SHAP analysis

In this research, we employed SHAP analysis to meticulously evaluate the significance of input features within the MLP and ConvFeatNet models. This analytical approach was designed to rigorously quantify the impact of each feature on the predictive accuracy of key material properties, namely Young's modulus, tensile strength, and fracture energy. The objective was to discern precisely how each feature contributes to the models' ability to forecast these critical mechanical characteristics, providing deeper insights into the data-driven decision-making process.

3.2.1. Weight shifting of MLP and CNN branches in ConvFeatNet

This segment of our study delves into the dynamics between the MLP and CNN branches within the ConvFeatNet architecture. Our investigation focuses on the changing influence of these branches as we progressively integrate larger amounts of training data, aiming to understand how each branch manages data of varying magnitudes and complexity.

Fig. 5(a) presents the SHAP values derived from test datasets through 5-fold cross-validation. These plots visually depict the evolution of the ConvFeatNet's weight allocations as it processes distinct physical properties. Solid lines indicate the mean cumulative significance of each branch, while shaded regions represent the confidence intervals at a 95 % confidence level.

Initial observations from Fig. 5(a)(i) indicate that the MLP branch plays a critical role when the model handles limited datasets, significantly influencing the predictions. However, as the volume of training data increases, the prominence of the MLP branch diminishes. This trend suggests that while the MLP is highly effective with smaller, more controlled datasets, its influence wanes as the CNN branch, which learns directly from the comprehensive and complex input microstructures, begins to dominate. This shift is due to the CNN's ability to directly assimilate and process intricate visual data from the input microstructures, outpacing the insights that the MLP can derive from feature-based learning. Consequently, when the dataset is small, the MLP's normalized importance stands high at around 0.8, but as data availability expands to encompass the entire dataset, this importance dwindles to about 0.3, highlighting the growing dominance of the CNN's capabilities.

Further analysis in Fig. 5(a)(ii) illustrates a plateauing effect in the significance of the MLP branch after incorporating 60 % of the training data, particularly for strength predictions. This plateau indicates a

Table 2

P-values from paired t-tests comparing the performance of different model pairs.

Comparison	p-value
MLP vs. ConvFeatNet	<0.0001
CNN vs. ConvFeatNet	0.0081
MLP vs. ConvFeatNet Ensemble	<0.0001
CNN vs. ConvFeatNet Ensemble	0.002
ConvFeatNet vs. ConvFeatNet Ensemble	<0.0001

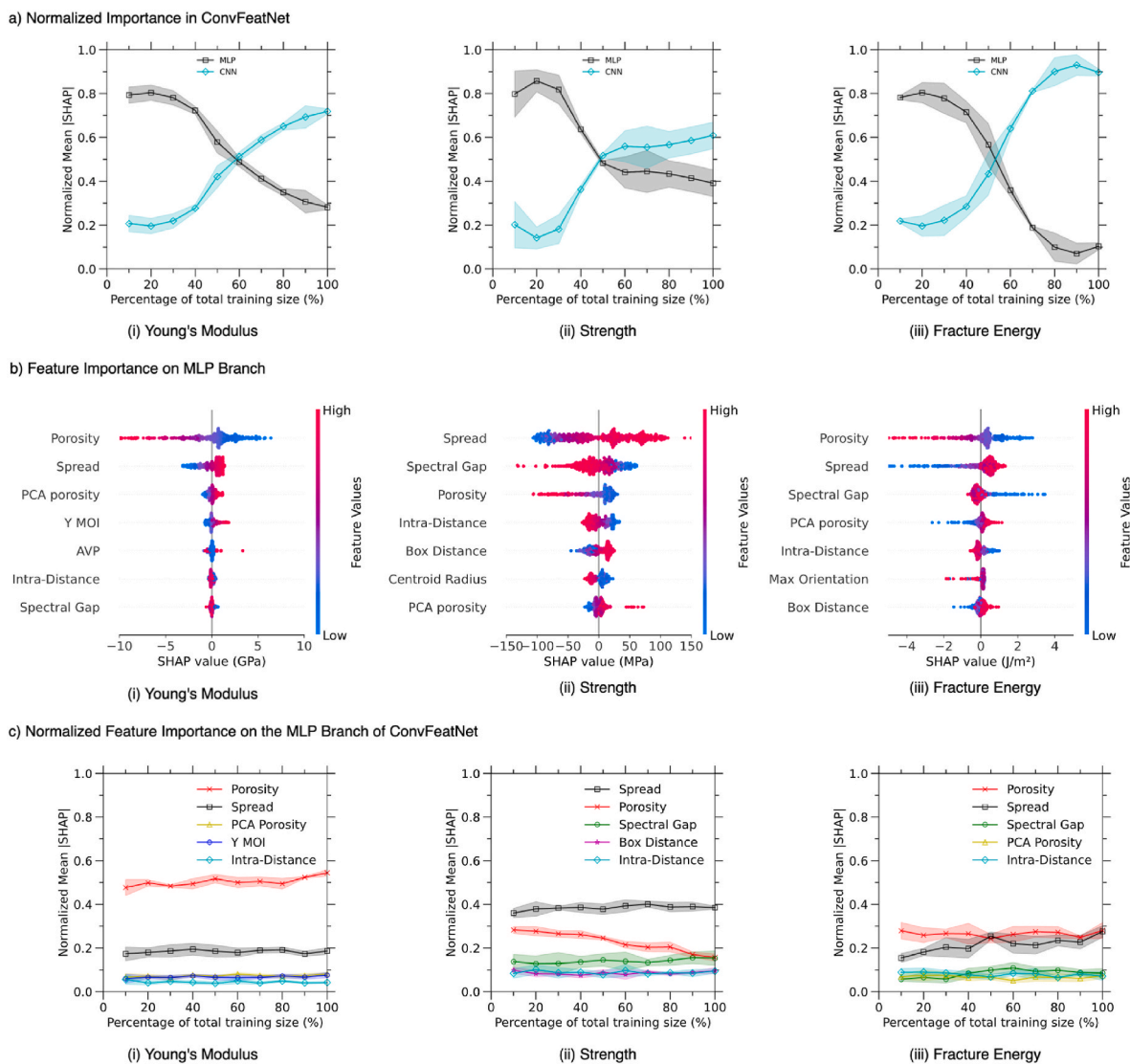


Fig. 5. SHAP Value Analysis of Feature Importance in ConvFeatNet's MLP Branch. This figure visualizes the distribution and impact of feature weights across different training datasets, as analyzed through SHAP values. Panel (a) presents a general view of the evolving importance of features in the MLP branch as the volume of training data increases, highlighting the dynamic interaction between the MLP and CNN branches within the model. Panel (b) details SHAP summary plots, ranking features by their importance in predicting physical properties like Young's modulus, strength, and fracture energy. Each dot represents a SHAP value for a specific instance of an input variable, with colors indicating the magnitude of impact. Panel (c) focuses on the normalized relevance of the top five features within the MLP branch, displaying mean absolute SHAP values and their confidence intervals across different dataset sizes. These plots collectively illustrate how local and global features influence the predictive performance of the model, underscoring the nuanced roles of porosity and spread in material property predictions. (For interpretation of the references to color in this figure legend, the reader is referred to the Web version of this article.)

robustness in the predictive features related to strength, which are not as readily overtaken by the CNN branch as those related to Young's modulus. The slight differences in mean values and the merging of confidence intervals between the branches underscore a nuanced competition that influences the final predictive outcomes.

In stark contrast, Fig. 5(a)(iii) showcases a significant divergence between the MLP and CNN branches when processing extensive datasets. Here, the CNN branch clearly outperforms the MLP, especially in predicting fracture energy, suggesting that the representations offered by the MLP become redundant with the availability of large datasets. This transition exemplifies the CNN's superior capability to harness and interpret data directly from the original grids, thereby overtaking the MLP's contributions as data richness increases.

3.2.2. Reliability of features

Fig. 5(b) provides SHAP summary plots that elucidate the relative importance of input features in predicting physical properties through

the MLP branch, using complete training sets. SHAP values are calculated based on cooperative game theory principles, where the contribution of each feature to the prediction is evaluated by considering all possible combinations of features. Specifically, the SHAP value of a feature represents the average marginal contribution of that feature to the prediction across all possible subsets of features.

In these plots, the y-axis displays the input variables in ascending order of their average SHAP values, indicating their significance in the prediction model. Each dot on the plot represents a SHAP value for a specific testing instance of an input variable, with a color gradient ranging from blue (representing lower variable values) to red (indicating higher variable values). This color gradient helps visualize how different values of a feature impact the prediction. The x-axis represents the SHAP values, showing how much each feature contributes to the deviation from the mean prediction of the target metric (e.g., fracture energy).

SHAP values themselves do not have units, instead, they are

expressed in the same units as the model's output. SHAP values are an abstract measure of the feature's contribution to the model's output. For example, a positive SHAP value indicates that the feature increases the prediction, while a negative SHAP value indicates that the feature decreases the prediction. By summing the SHAP values of all features for a specific instance, we obtain the difference between the model's prediction for that instance and the mean prediction.

In Fig. 5(b)(i), the pivotal role of porosity in influencing Young's modulus is clearly demonstrated, affirming established literature that links higher porosity with decreased Young's modulus in porous materials [44]. This plot reinforces the sensitivity of Young's modulus to porosity variations within the material structure.

Fig. 5(b)(ii) emphasizes the importance of the feature 'spread' in predicting material strength, showcasing a direct correlation where increased feature values correspond with higher SHAP values. This plot also notes the significance of the spectral gap and porosity, which closely follow 'spread' in their predictive importance [45–47].

Spectral gap measures the connectivity of the pore network, which influences how stress propagates through the material. Our results demonstrate that a higher spectral gap correlates with lower tensile strength, as highly fragmented pore structures create stress localization points that accelerate failure. Conversely, a lower spectral gap indicates better connectivity between solid regions, enhancing load transfer and improving tensile strength. Similar behavior has been observed in high-carbon steels, where reduced pore fragmentation increases ductility and tensile performance [17]. Graph-based material models further confirm that spectral gap serves as an indicator of mechanical stability in heterogeneous structures [34].

In Fig. 5(b)(iii), the analysis highlights how both porosity and spread crucially affect fracture energy predictions. Lower SHAP values associated with higher porosity and reduced spread suggest these features substantially decrease the fracture energy. This behavior is attributed to the mechanics within the porous region, especially in the pre-cracked area (PCA) and non-cracked area (NCA). The interconnected pores, akin to pre-existing cracks, diminish stress concentration at the fracture tip, thereby requiring higher stress levels to reach critical stress concentrations for fracture propagation [48,49,50]. This dynamic leads to a redistribution of stress, enhancing material strength due to the heterogeneous elasticity contributed by uneven pore distribution, which mimics the behavior of 'soft inclusions' within the material matrix. As fractures progress, these inclusions deflect cracks significantly, thereby increasing the actual crack area and the energy absorbed during fracture [51,52].

In addition, we also observed that PCA porosity, which means the porosity within the PCA, has a positive impact on fracture energy. The presence of voids in the PCA cause localized stress concentrations that delay crack propagation, requiring more energy to initiate and propagate fractures. The PCA serves as an energy dissipation zone, increasing the material's capacity to absorb external loads before catastrophic failure. This effect is particularly relevant for materials with irregular or engineered porous microstructures, where the voids near the initial crack tip influence energy absorption mechanisms during crack initiation and propagation. For example, researchers found that the presence of intentionally placed voids near the crack tip contributes to improved fracture energy by increasing the material's resistance to crack growth [53]. Similarly, experiments on cellular structures show that controlled porosity in the PCA enhances fracture toughness by dissipating more energy as cracks propagate through the material [54]. These studies underscore the significant influence of PCA porosity, especially in terms of its distribution near the crack tip, on fracture behavior.

3.2.3. Feature weights within ConvFeatNet's MLP branch

This segment of our research delves into the analysis of feature weights within the MLP branch of the ConvFeatNet architecture, aiming to determine their relative significance in predicting material properties. Fig. 5(c) presents the normalized relevance of the top five features as

determined through validation datasets, where the vertical axis shows the mean absolute SHAP values for each feature, surrounded by shaded regions depicting the 95 % confidence intervals established via 5-fold cross-validation.

Notably, Fig. 5(c)(i) demonstrates the significant influence of porosity on the predictions of Young's modulus. The consistency of porosity's normalized significance at around 0.5 across all dataset sizes aligns with the well-documented inverse relationship between the porosity of porous materials and their Young's modulus. This finding underscores the critical role of porosity in structural integrity assessments and material specification.

In Fig. 5(c)(ii), the feature known as 'spread' shows a marginal increase in importance as more training data is incorporated, highlighting its nuanced role in the predictive model. Contrarily, the significance of porosity decreases with the introduction of more extensive data, suggesting that while porosity is a dominant factor in smaller or more specific datasets, its influence becomes diluted as the diversity and volume of data expand. Despite this, other global features generally show a minimal impact in larger datasets, whereas local features like spread continue to be significant. This trend suggests that local structural properties, which often involve complex spatial relationships like the distance between voids, present ongoing challenges for model comprehension and require nuanced representation within the neural network.

The persistent relevance of these local features, as shown in Fig. 5(c)(iii), where weights of local characteristics increase with more data, indicates that while the CNN branch of ConvFeatNet significantly enhances model learning from graphical data, it does not entirely overshadow the contributions of intricate local features processed by the MLP branch. This enduring influence highlights the complementary nature of the dual-branch system in ConvFeatNet, where both global and local features are integrated to provide a comprehensive understanding of material properties.

Overall, the insights gained from the feature weight analysis in the MLP branch reveal the intricate balance between global and local features in material prediction models. The interplay between these feature types helps refine the model's accuracy and adaptability, ensuring that ConvFeatNet remains robust and effective across varying scales of data complexity.

3.3. Trade-offs between computational cost and accuracy

Recent advances in deep learning methods in materials science [55, 56] have shown that while simpler models like MLPs train very quickly, they plateau in predictive performance. In contrast, more complex architectures such as CNNs and ensemble models can extract hierarchical features from spatially structured data and achieve significantly lower prediction errors, even though they require substantially more computational resources. This observation is reinforced by a recent methodological survey in materials informatics [57] that demonstrates an efficiency–accuracy Pareto frontier: simpler models provide rapid screening with moderate accuracy, while deep ensembles deliver superior precision at 4–6 × higher computational costs. Furthermore, experimental studies on ensemble deep graph networks [58] have quantified that ensemble approaches can reduce prediction errors by 18–22 % compared to individual models, albeit with increased training time and memory overhead.

In our study, we evaluated four models—MLP, CNN, ConvFeatNet, and ConvFeatNet Ensemble—using training datasets of 1000 and 10,000 samples. All models trained on identical data partitions. At the 1000-sample level, the MLP model required only about 89 s in total (1.78 s per epoch over 50 epochs) and achieved a fracture energy MAE of 1.07 J/m². In contrast, the ConvFeatNet Ensemble, which trains at 38.02 s per epoch for 70 epochs (approximately 2661 s total), reached a significantly lower fracture energy MAE of 0.85 J/m². The CNN and single ConvFeatNet models occupied intermediate positions in both training

Table 3

Summary of training times and mean absolute errors (MAEs) for MLP, CNN, ConvFeatNet, and ConvFeatNet Ensemble when using 1000 and 10,000 samples.

1000 Samples						
Model	Time/Epoch (s)	# Epochs	Total Time (s)	Young's modulus MAE (GPa)	Strength MAE (MPa)	Fracture Energy MAE (J/m ²)
MLP	1.78	50	89.0	0.621	2.72	1.07
CNN	3.24	70	226.8	0.906	3.25	1.39
ConvFeatNet	6.08	70	425.6	0.563	2.71	1.08
ConvFeatNet Ensemble	38.02	70	2661.4	0.572	2.48	0.85
10,000 Samples						
Model	Time/Epoch (s)	# Epochs	Total Time (s)	Young's modulus MAE (GPa)	Strength MAE (MPa)	Fracture Energy MAE (J/m ²)
MLP	18.01	100	1801.0	0.553	2.29	0.675
CNN	32.52	350	11,382.0	0.437	1.95	0.560
ConvFeatNet	53.00	350	18,550.0	0.392	1.94	0.555
ConvFeatNet Ensemble	192.00	350	67,200.0 (~18.7 h)	0.366	1.91	0.517

time and predictive performance.

When we increased the dataset size to 10,000 samples, the MLP's performance showed little improvement (fracture energy MAE of 0.675 J/m²), likely because its predefined feature representations limit further gains. Conversely, the CNN, ConvFeatNet, and particularly the ConvFeatNet Ensemble continued to improve, with the ensemble achieving a fracture energy MAE of 0.517 J/m². However, this enhancement came at a steep computational cost—the ensemble model required roughly 67,200 s (about 18.7 h) of total training time, compared to only 1801 s (about 30 min) for the MLP.

These results have important practical implications. For resource-constrained settings or applications where rapid prototyping is critical, such as early-stage materials research or embedded systems, faster models like the MLP or a single ConvFeatNet may be preferable despite their slightly higher error rates. In contrast, for high-stakes industrial applications (e.g., aerospace, defense, or critical infrastructure) where even modest improvements in prediction accuracy can have significant safety or economic impacts, the additional computational expense of ensemble methods is justified.

The findings of our study are summarized in the Table 3 below.

These empirical results, together with the insights provided in recent literature [56–58], support the conclusion that while ensemble approaches (e.g., ConvFeatNet Ensemble) yield substantial improvements in predictive accuracy, they demand significantly greater computational resources. Consequently, the choice of model should be guided by the specific application context—favoring rapid, low-cost models for prototyping and resource-limited environments, and high-accuracy ensembles for critical, high-stakes applications.

4. Conclusion

This study has successfully developed a comprehensive model for predicting the mechanical properties of porous materials by leveraging their microstructural configurations along with domain-specific extracted features. This innovative approach enables accurate predictions of Young's modulus, strength, and fracture energy across varying scales of training data.

To mitigate the extensive data demands typically associated with Convolutional Neural Networks (CNNs), our methodology uniquely integrates these networks with a Multilayer Perceptron (MLP) branch. This MLP branch is meticulously designed to process predetermined features, allowing for the effective extraction of vital structural and chemical information pertinent to specific material qualities.

Building on the foundations laid by our individual model components, we further introduced the ConvFeatNet ensemble. This advanced ensemble technique significantly enhances the reliability and accuracy of our predictions, consistently outperforming all baseline benchmarks across the three examined physical properties.

Moreover, the validity and robustness of our feature selection and the model's interpretative capabilities are confirmed through SHAP

analysis. This analysis not only corroborates our model's predictions but also aligns seamlessly with established theoretical understanding of the material properties under study.

In essence, the integration of MLP and CNN within the ConvFeatNet framework, complemented by the ensemble approach, represents a significant advancement in the field of materials science. It offers a robust predictive tool that combines deep learning efficiency with expert knowledge, setting a new standard for accuracy and reliability in material property predictions.

Use of AI

We utilized an AI-based language model to improve the readability of the manuscript. This tool assisted in proofreading, ensuring that the text is presented in a clear and professional manner.

CRediT authorship contribution statement

Yuhai Li: Writing – review & editing, Writing – original draft, Visualization, Software, Methodology, Investigation, Formal analysis, Data curation, Conceptualization. **Tianmu Li:** Writing – review & editing, Supervision, Methodology, Conceptualization. **Longwen Tang:** Writing – review & editing, Supervision, Conceptualization. **Shiyu Ma:** Methodology. **Qinglin Wu:** Methodology. **Puneet Gupta:** Writing – review & editing, Validation, Supervision, Conceptualization. **Mathieu Bauchy:** Writing – review & editing, Supervision, Funding acquisition, Conceptualization.

Declaration of competing interest

The authors declare that there are no conflicts of interest or competing interests regarding the publication of this paper entitled “ConvFeatNet Ensemble: Integrating Microstructure and Pre-defined Features for Enhanced Prediction of Porous Material Properties.” The research was conducted in the absence of any commercial or financial relationships that could be construed as a potential conflict of interest.

All authors have approved the manuscript and agree with its submission to Materials Science and Engineering: A. The research reported in this manuscript complies with ethical standards and has not been published previously nor is it under consideration for publication elsewhere.

Additionally, we confirm that the datasets generated and/or analyzed during the current study are available from the corresponding author on reasonable request.

Appendix A. Supplementary data

Supplementary data to this article can be found online at <https://doi.org/10.1016/j.msea.2025.148173>.

Data availability

Data will be made available on request.

References

- [1] M.E. Davis, Ordered porous materials for emerging applications, *Nature* 417 (6891) (2002) 813–821.
- [2] A.J.D. Shaikeea, H. Cui, M. O'Masta, X.R. Zheng, V.S. Deshpande, The toughness of mechanical metamaterials, *Nat. Mater.* 21 (3) (2022) 297–304.
- [3] P.P. Camanho, C.G. Davila, M.F. De Moura, Numerical simulation of mixed-mode progressive delamination in composite materials, *J. Compos. Mater.* 37 (16) (2003) 1415–1438.
- [4] D.C. Hofmann, J.Y. Suh, A. Wiest, G. Duan, M.L. Lind, M.D. Demetriou, W. L. Johnson, Designing metallic glass matrix composites with high toughness and tensile ductility, *Nature* 451 (7182) (2008) 1085–1089.
- [5] Z. Chen, Z. Li, J. Li, C. Liu, C. Lao, Y. Fu, Y. He, 3D printing of ceramics: a review, *J. Eur. Ceram. Soc.* 39 (4) (2019) 661–687.
- [6] J.Y. Lee, J. An, C.K. Chua, Fundamentals and applications of 3D printing for novel materials, *Appl. Mater. Today* 7 (2017) 120–133.
- [7] J. Jancar, J.F. Douglas, F.W. Starr, S.K. Kumar, P. Cassagnau, A.J. Lesser, M. J. Buehler, Current issues in research on structure–property relationships in polymer nanocomposites, *Polymer* 51 (15) (2010) 3321–3343.
- [8] R.F. Gibson, A review of recent research on mechanics of multifunctional composite materials and structures, *Compos. Struct.* 92 (12) (2010) 2793–2810.
- [9] C. Chen, Y. Kuang, S. Zhu, I. Burgert, T. Keplinger, A. Gong, L. Hu, Structure–property–function relationships of natural and engineered wood, *Nat. Rev. Mater.* 5 (9) (2020) 642–666.
- [10] P. Ball, Concrete mixing for gorillas, *Nat. Mater.* 14 (5) (2015), 472–472.
- [11] V.C. Li, S. Wang, C. Wu, Tensile strain-hardening behavior of polyvinyl alcohol engineered cementitious composite (PVA-ECC), *Mat. J.* 98 (6) (2001) 483–492.
- [12] H. Hu, L. Qi, X. Chao, Physics-informed Neural Networks (PINN) for computational solid mechanics: numerical frameworks and applications, *Thin-Walled Struct.* (2024) 112495.
- [13] A.K. Chew, M. Sender, Z. Kaplan, A. Chandrasekaran, J. Chief Elk, A.R. Browning, M.A.F. Afzal, Advancing material property prediction: using physics-informed machine learning models for viscosity, *J. Cheminf.* 16 (1) (2024) 31.
- [14] J. Willard, X. Jia, S. Xu, M. Steinbach, V. Kumar, arXiv preprint arXiv:2003.04919, Integrating Physics-Based Modeling with Machine Learning: A Survey, vol. 1, 2020, pp. 1–34, 1.
- [15] Q. Liang, P. Han, E. Vanem, K. Erik Knutsen, H. Zhang, A hybrid approach integrating physics-based models and expert-augmented neural networks for ship fuel consumption prediction, *J. Offshore Mech. Arctic Eng.* 147 (3) (2025).
- [16] S. Kasilingam, R. Yang, S.K. Singh, M.A. Farahani, R. Rai, T. Wuest, Physics-based and data-driven hybrid modeling in manufacturing: a review, *Production Manufact. Res.* 12 (1) (2024) 2305358.
- [17] H. Wang, D. Qian, F. Wang, Z. Dong, J. Chen, Predictive mechanical property and fracture behavior in high-carbon steel containing high-density carbides via artificial RVE modeling, *Mater. Des.* 247 (2024) 113383.
- [18] A.A. Emery, J.E. Saal, S. Kirklind, V.I. Hegde, C. Wolverton, High-throughput computational screening of perovskites for thermochemical water splitting applications, *Chem. Mater.* 28 (16) (2016) 5621–5634.
- [19] V. Botu, R. Ramprasad, Adaptive machine learning framework to accelerate ab initio molecular dynamics, *Int. J. Quant. Chem.* 115 (16) (2015) 1074–1083.
- [20] K.T. Butler, D.W. Davies, H. Cartwright, O. Isayev, A. Walsh, Machine learning for molecular and materials science, *Nature* 559 (7715) (2018) 547–555.
- [21] K. Hansen, G. Montavon, F. Biegler, S. Fazli, M. Rupp, M. Scheffler, K.R. Muller, Assessment and validation of machine learning methods for predicting molecular atomization energies, *J. Chem. Theor. Comput.* 9 (8) (2013) 3404–3419.
- [22] A. Mannodi-Kanakithodi, G. Pilania, T.D. Huan, T. Lookman, R. Ramprasad, Machine learning strategy for accelerated design of polymer dielectrics, *Sci. Rep.* 6 (1) (2016) 20952.
- [23] P. Avery, X. Wang, C. Oses, E. Gossett, D.M. Proserpio, C. Toher, E. Zurek, Predicting superhard materials via a machine learning informed evolutionary structure search, *npj Comput. Mater.* 5 (1) (2019) 89.
- [24] S. Kumar, S. Tan, L. Zheng, D.M. Kochmann, Inverse-designed spinodoid metamaterials, *npj Comput. Mater.* 6 (1) (2020) 73.
- [25] K. Yang, X. Xu, B. Yang, B. Cook, H. Ramos, N.A. Krishnan, M. Bauchy, Predicting the Young's modulus of silicate glasses using high-throughput molecular dynamics simulations and machine learning, *Sci. Rep.* 9 (1) (2019) 8739.
- [26] C. Wang, H. Fu, L. Jiang, D. Xue, J. Xie, A property-oriented design strategy for high performance copper alloys via machine learning, *npj Comput. Mater.* 5 (1) (2019) 87.
- [27] C. Ma, Z. Zhang, B. Luce, S. Pusateri, B. Xie, M.H. Rafiei, N. Hu, Accelerated design and characterization of non-uniform cellular materials via a machine-learning based framework, *npj Comput. Mater.* 6 (1) (2020) 40.
- [28] X. Liu, C.E. Athanasiou, N.P. Padture, B.W. Sheldon, H. Gao, A machine learning approach to fracture mechanics problems, *Acta Mater.* 190 (2020) 105–112.
- [29] G.X. Gu, C.T. Chen, D.J. Richmond, M.J. Buehler, Bioinspired hierarchical composite design using machine learning: simulation, additive manufacturing, and experiment, *Mater. Horiz.* 5 (5) (2018) 939–945.
- [30] G.X. Gu, C.T. Chen, M.J. Buehler, De novo composite design based on machine learning algorithm, *Extreme Mech. Lett.* 18 (2018) 19–28.
- [31] Y. Wang, M. Zhang, A. Lin, A. Iyer, A.S. Prasad, X. Li, L.C. Brinson, Mining structure–property relationships in polymer nanocomposites using data driven finite element analysis and multi-task convolutional neural networks, *Molecul. Syst. Design Eng.* 5 (5) (2020) 962–975.
- [32] H. Chan, M. Cherukara, T.D. Loeffler, B. Narayanan, S.K. Sankaranarayanan, Machine learning enabled autonomous microstructural characterization in 3D samples, *npj Comput. Mater.* 6 (1) (2020) 1.
- [33] Y. Xiang, Z. Wang, S. Zhang, L. Jiang, Y. Lin, J. Tan, Cross-sectional performance prediction of metal tubes bending with tangential variable boosting based on parameters-weight-adaptive CNN, *Expert Syst. Appl.* 237 (2024) 121465.
- [34] Y. Su, J. Zhu, X. Long, L. Zhao, C. Chen, C. Liu, Statistical effects of pore features on mechanical properties and fracture behaviors of heterogeneous random porous materials by phase-field modeling, *Int. J. Solid Struct.* 264 (2023) 112098.
- [35] S.M. Lundberg, S.I. Lee, A unified approach to interpreting model predictions, *Adv. Neural Inf. Process. Syst.* 30 (2017).
- [36] F. Rao, L. Tang, Y. Li, G. Ye, C. Hoover, Z. Zhang, M. Bauchy, Stochastic micromechanical damage model for porous materials under uniaxial tension, *J. Mater. Civ. Eng.* 34 (4) (2022) 04022018.
- [37] G. Rogers, *The Nature of Engineering*, 2021.
- [38] J.L. Jensen, M. Nakatani, P. Quenneville, B. Walford, A Simple Unified Model for Withdrawal of Lag Screws and Glued-In Rods, 2011.
- [39] P. Hajikarimi, F.M. Nejad, Applications of Viscoelasticity: Bituminous Materials Characterization and Modeling, Elsevier, 2021.
- [40] S.A. Silling, M. Epton, O. Weckner, J. Xu, E. Askari, Peridynamic states and constitutive modeling, *J. Elasticity* 88 (2007) 151–184.
- [41] D.P. Kingma, J. Ba, Adam: A Method for Stochastic Optimization, 2014 arXiv preprint arXiv:1412.6980.
- [42] X. Glorot, Y. Bengio, Understanding the difficulty of training deep feedforward neural networks, in: Proceedings of the Thirteenth International Conference on Artificial Intelligence and Statistics, JMLR Workshop and Conference Proceedings, 2010, March, pp. 249–256.
- [43] D. Ciregan, U. Meier, J. Schmidhuber, Multi-column deep neural networks for image classification, in: 2012 IEEE Conference on Computer Vision and Pattern Recognition, IEEE, 2012, June, pp. 3642–3649.
- [44] S. De Carolis, C. Putignano, L. Soria, G. Carbono, Effect of porosity and pore size distribution on elastic modulus of foams, *Int. J. Mech. Sci.* 261 (2024) 108661.
- [45] K.K. Yaswanth, V.S. Vani, K. Biswal, G.P. Kumar, C. Manjula, S. Govindarajan, U. Prameela, A critical analysis of compressive strength prediction of glass fiber and carbon fiber reinforced concrete over machine learning models, *Multiscale Multidisciplinary Model. Exp. Des.* 8 (3) (2025) 178.
- [46] S. Achra, R. Nagar, R. Kumar, R. Gupta, Application of non-destructive methods for predicting the concrete's compressive strength, using hyper-tuned machine learning techniques, *Iranian J. Sci. Technol. Transact. Civil Eng.* (2025) 1–17.
- [47] Shobijan, J., Ahilash, N., Wijekoon, S. H. B., & Subramaniam, D. N. Prediction of Impact of Aggregate Shape on Pervious Concrete Compressive Strength.
- [48] Z.Q. Ma, X.Y. Yin, Z.Y. Zong, Y.Y. Tan, Y.M. Yang, Analytical solution for the effective elastic properties of rocks with the tilted penny-shaped cracks in the transversely isotropic background, *Pet. Sci.* 21 (1) (2024) 221–243.
- [49] D.K.L. Tsang, S.O. Oyadiji, A.Y.T. Leung, Multiple penny-shaped cracks interaction in a finite body and their effect on stress intensity factor, *Eng. Fract. Mech.* 70 (15) (2003) 2199–2214.
- [50] M. Huang, L. Wang, C. Wang, Y. Li, J. Wang, J. Yuan, W. Xu, Optimizing crack initiation energy in austenitic steel via controlled martensitic transformation, *J. Mater. Sci. Technol.* 198 (2024) 231–242.
- [51] L. Tang, N.A. Krishnan, J. Berjikian, J. Rivera, M.M. Smedskjaer, J.C. Mauro, M. Bauchy, Effect of nanoscale phase separation on the fracture behavior of glasses: toward tough, yet transparent glasses, *Phys. Rev. Mater.* 2 (11) (2018) 113602.
- [52] Z.D. Fan, H.P. Xie, X. Sun, R. Zhang, C.B. Li, Z.T. Zhang, L. Ren, Crack deflection in shale-like layered rocks under three-point bend loading, *Eng. Fract. Mech.* 289 (2023) 109464.
- [53] F. Zhou, Q. Xin, Y. Fu, Z. Hua, Y. Dong, M. Ran, X. Gao, Efficient catalytic oxidation of chlorinated volatile organic compounds over RuO₂-WO_x/SnO₂. 2TiO₂. 8O₂ catalysts: insight into the Cl poisoning mechanism of acid sites, *Chem. Eng. J.* 464 (2023) 142471.
- [54] Z. Jiang, G. He, Y. Duan, Y. Jiang, Y. Lin, Y. Zhu, J. Wang, Contrasting effects of various factors upon the properties of foam ceramics and the mechanisms of crystalline phase reconstruction and microstructure regulation, *Ceram. Int.* 50 (12) (2024) 21645–21657.
- [55] D. Ren, C. Wang, X. Wei, Y. Zhang, S. Han, W. Xu, Harmonizing physical and deep learning modeling: a computationally efficient and interpretable approach for property prediction, *Scr. Mater.* 255 (2025) 116350.
- [56] K. Choudhary, B. DeCost, C. Chen, A. Jain, F. Tavazza, R. Cohn, C. Wolverton, Recent advances and applications of deep learning methods in materials science, *npj Comput. Mater.* 8 (1) (2022) 59.
- [57] C. Li, K. Zheng, Methods, progresses, and opportunities of materials informatics, *InfoMat* 5 (8) (2023) e12425.
- [58] C.M.A. Rahman, G. Bhandari, N.M. Nasrabadi, A.H. Romero, P.K. Gyawali, Enhancing material property prediction with ensemble deep graph convolutional networks, *Front. Mat.* 11 (2024) 1474609.